Synthesis of Ce-doped magnetic biochar for effective Sb(V) removal: Performance and mechanism

Li Wang [a,*], Jingyi Wang [a], Zixuan Wang [a,b], Jiangtao Feng [a], Shanshan Li [a], Wei Yan [a,*]

[a] Department of Environmental Science and Engineering, State Key Laboratory of Multiphase Flow in Power Engineering, School of Energy and Power Engineering, Xi'an Jiaotong University, Xi'an 710049, China
[b] Department of Civil and Environmental Engineering, Virginia Polytechnic Institute and State University, Blacksburg, VA 24061, USA

ABSTRACT

A novel Ce-doped magnetic biochar was successfully synthesized by chemical co-precipitation (Ce/Fe$_{CP}$-BC) and solvothermal methods (Ce/Fe$_{ST}$–BC) for efficient Sb(V) adsorption. The Ce/Fe$_{CP}$-BC exhibited a high adsorption capacity of 25.0 mg/g, which was two times and one order of magnitude higher than that of Ce/Fe$_{ST}$-BC and un-doped BC, respectively. The excellent adsorption performance of Ce/Fe$_{CP}$-BC maintained over a wide pH range or in the presence of coexisting anions. The adsorption results indicated that co-precipitation method was superior to solvothermal method and Ce oxide was the main contribution to Sb(V) adsorption enhancement. The combined results of TEM, XRD, FTIR and XPS revealed that Ce atom was successfully doped into the Fe$_3$O$_4$ structure and abundant hydroxyl groups were formed on the surface of Ce/Fe$_{CP}$-BC. The magnetic performance decreased after Ce doping, but Ce/Fe$_{CP}$-BC still showed good separation potential. Based on the results of batch experiments and physiochemical analyses, the underlying mechanisms controlling Sb(V) adsorption on Ce/Fe$_{CP}$-BC involved the inner-sphere surface complexation, hydrogen bonding, electrostatic attraction and ligand exchange. Among them, the ligand exchange and the formation of Ce–O–Sb complex were the main contributions to the significant Sb(V) adsorption increment on Ce/Fe$_{CP}$-BC. All the results implied that Ce/Fe$_{CP}$-BC could be used as a promising adsorbent for antimonate decontamination.

© 2019 Elsevier B.V. All rights reserved.

1. Introduction

Antimony (Sb) contamination in aqueous systems has been causing growing concern due to environmental threats posed from its bio-accumulation, poor degradability and environmental persistence [1]. The elevated concentrations of antimony in water environment (ppm level) are normally derived from the production of various industrial products such as flame retardants, semiconductors, batteries and plastics as well as the process of mining, smelting, and metallurgy [2]. Long-term exposure to antimony could result in various illnesses such as skin rashes, myalgia, diarrhea, abdominal colic and cardiotoxicity [3]. To minimize its potential threats, the United States Environmental Protection Agency (USEPA, 1979) regulated the stringent limit of 6 μg/L, with 5 μg/L set in EU and China, as the maximum permissible antimony level in drinking water [4]. In addition, Sb(III) and Sb(V) are the oxidation states of Sb in the natural environment, with the usual forms of Sb(OH)$_3$ and [Sb(OH)$_6$]$^−$ in relatively reducing and oxidizing water environment respectively [2]. Although the toxicity of Sb(III) is 10 times greater than that of Sb(V), the mobility, stability and solubility of Sb(V) are greater than Sb(III) in Sb polluted wastewater that mostly stays in an oxidizing environment [5].

An extensive literature survey reveals that numerous techniques have been applied to antimony removal from water environment [5,6], among which adsorption is normally deemed to be a superior technique because of its high efficiency, cost effectivity and operational simplicity [6–8]. Recently, biochar as a novel adsorbent has received considerable interest for the removal of heavy metals from wastewater due to its low cost and eco-friendly features as well as unique properties such as large surface area, high porosity, and various surface functional groups [9–11]. Various types of biomass (e.g., agricultural waste, wood chips, algae, manure, sewage sludge, etc.) have been reported to be used as precursors for BC preparation under oxygen-limited pyrolysis conditions [12–14]. Despite that, the surface of the pristine biochar (BC) is generally negative charged, which is not favorable for the adsorption of anionic contaminants [15]. Moreover, the large-scale use of BC is quite limited because of the difficulties entailed in the separation of powdered adsorbents [16]. Therefore, suitable modification of BC is required.

Magnetic separation is an excellent option for easy separation of adsorbents from aqueous solutions. Fe$_3$O$_4$ is one of the most commonly used magnetic materials to endow the BC with magnetic property [17–19]. However, its specific adsorption affinity towards Sb(V) still

remains to be improved. Recently, various transition metal elements have gained increasing attention for the adsorption of Sb(V) from aqueous solutions [20–22]. For instance, a Fe—Zr bimetal oxide fabricated via co-precipitation method exhibited significant enhancement in Sb (V) removal compared to the referenced ferric oxide [23]. In contrast to the pure Fe_3O_4, Cu-Fe_3O_4 nanoparticle prepared by solvothermal method increased Sb(V) adsorption capacity from 7.09 mg/g to 30.92 mg/g [24].

Cerium (Ce), one of the most abundant and the least expensive rare earth metals, has been proved that the presence of Ce ions makes adsorbent surface more positively charged, which would contribute to attract the negative adsorbates [25] such as arsenate, chromate, phosphate and fluoride [26,27]. Besides, numerous hydroxyl groups could be normally formed on the surface of Ce-doped adsorbents and displaced by certain anions, which would lead to the excellent specific adsorption performance [28]. It has been demonstrated that the Ce-doped Fe_3O_4 showed a dramatically higher As(V) adsorption capacity than pure Fe_3O_4 [29]. As Sb and As both locate in VA group with similar structure, Ce could be used as a good doping element to improve Sb removal efficiency. However, pure metal oxide nanoparticles are inclined to agglomerate during the synthesis and adsorption process, which may decrease their removal efficiency and stability [30]. Given these issues, combining Ce-doped Fe_3O_4 and BC matrix is an excellent option for facilitating the dispersion degree of metal oxides, Sb(V) adsorption performance as well as easy separation. Until now, no systematic study concerning the adsorption performance of Ce-doped magnetic BC in Sb(V) removal from aquatic environment has been published yet.

Chemical co-precipitation and solvothermal methods are two commonly used methods for the development of metal oxide nanoparticles or metal modified BCs as extensively reported in literature [23,24], leading to different morphologies of the materials. In view of the above considerations, the main aims of the research are to 1) synthesize Ce-doped magnetic BCs via two different methods (co-precipitation and solvothermal method); 2) compare and evaluate their aqueous Sb (V) adsorption performances as well as mechanisms involved through a series of batch experiments and BET, zeta potential, XRD, FTIR and XPS analyses.

2. Materials and methods

2.1. Adsorbent preparation

Phragmites australis (PA), a common hydrophyte, was used as the biomass precursor for BC preparation. PA was collected from Chan Ba wetland, Shaanxi province, China. The biomass was first cleaned with deionized water and dried at 80 °C for one day. Then the sample was pulverized into small pieces and heated in a microwave oven (MKX-M1B, Qingdao, China) at 700 W (600 °C) for 20 min under N_2 atmosphere. After that, the sample was cooled down to room temperature and ground to sieve through 200 meshes [31,32], then the pristine BC was acquired.

The Ce-doped magnetic BCs were synthesized by two methods: chemical co-precipitation (Ce/Fe$_{CP}$-BC) and solvothermal method (Ce/Fe$_{ST}$-BC). Specifically, $CeCl_3 \cdot 7H_2O$ (0.46 g), $FeCl_3 \cdot 6H_2O$ (0.76 g) and $FeCl_2 \cdot 4H_2O$ (0.27 g) in a molar ratio of 0.3 (Ce:Fe) were dissolved in 50 mL deionized water under vigorous stirring to form a homogeneous solution. Then 2.0 g of BC with 10 mL ethyl alcohol as the dispersing agent was added to the solution and stirred at room temperature for 2 h. The pH of the suspension was adjusted to 10 by adding about 2.5 mL ammonia solution (28% in H_2O) dropwise. In the synthesis of Ce/Fe$_{CP}$-BC sample, the mixture was shaken in a water bath shaker (THZ-82) at 80 °C (180 rpm) for another 2 h. In the synthesis of Ce/Fe$_{ST}$-BC sample, the mixture was transferred into a stainless Teflon lined autoclave. The autoclave was sealed and maintained at 180 °C for 12 h [25]. After being naturally cooled down to room temperature, the two products were washed several times with deionized water

until the pH reached 7. Then the products were separated and dried in an oven at 60 °C for 12 h. All the products were ground to pass through a 200 mesh sieve and stored in sealed bottles respectively for further use.

The supernatant was filtrated and the residual concentrations of Ce and Fe were detected by inductively coupled plasma emission spectrometer (ICPE-9000, Shimadzu Company, Japan). Results showed that all the Ce and Fe were loaded on the BC' s surface as no Ce or Fe ions were detected. For comparison, un-doped Fe-BC was also synthesized using the same method as Ce/Fe$_{CP}$-BC without adding $CeCl_3 \cdot 7H_2O$. All the chemicals used in this work are of analytical grade and solutions were prepared with deionized water.

2.2. Batch experiments

The adsorption performances of the modified BCs were investigated through a series of batch experiments. The effects of initial Sb (V) concentration (10.0–100.0 mg/L), contact time, initial solution pH (2.0–12.5) and coexisting anions (Cl^-, SO_4^{2-}, NO_3^-, HCO_3^-, $H_2PO_4^-$) on the removal of Sb(V) were studied successively. The stock solution of 500 mg/L Sb(V) ions was prepared by dissolving $KSbO_6H_6$ (1.079 g) in 1.0 L of deionized water. The solutions of required concentrations for subsequent tests were freshly prepared before use by diluting the stock solution with deionized water and adjusting pH using HCl and NaOH solutions (0.001 to 2.0 mol/L).

The batch adsorption equilibrium experiments were performed in 50 mL polypropylene centrifuge tubes by shaking 0.02 g of each adsorbent in 20 mL Sb(V) solution with a certain pH and concentration. All the adsorption experiments were carried out in a thermostatic shaker (150 rpm) at 25 °C for 15 h to reach equilibrium. For the adsorption kinetic experiment, 0.2 g each adsorbent was added into 200 mL Sb (V) solution with an initial concentration of 50 mg/L. About 2.0 mL of the solution was taken out at predetermined time intervals (1, 3, 7, 10, 15, 21, 28, 36, 45, 55, 70, 90, 120, 150, 180, 240, 300, 360, 450, 600 min). Afterwards, each sample was separated by a 0.45 μm membrane filter. The residual Sb(V) concentration was also measured by ICPE, in which the detection limit of Sb was 0.03 mg/L. The adsorption amount of Sb(V) at equilibrium was calculated as: $Q_e = (C_0 - C_e)V/W$, where Q_e represents the adsorption amount (mg Sb(V)/g adsorbent) at equilibrium, C_0 and C_e are Sb(V) concentrations at the initial moment and equilibrium (mg/L), respectively; V is the solution volume (L); and W is the adsorbent mass (g). The adsorption amount at time t, that is, Q_t (mg/g), was calculated as: $Q_t = (C_0 - C_t)V/W$, where C_0 and C_t (mg/L) are Sb(V) concentrations at the initial moment and time t, respectively; V is the solution volume (L); and W is the adsorbent mass (g). The adsorption isotherms were analyzed by Langmuir, Freundlich and Dubinin–Radushkevich isotherm (D-R) models, their equations were shown in Eqs. (S1)–(S3). The batch kinetic data were calculated using pseudo-first order, pseudo-second order, elovich and intra-particle diffusion models by Eqs. (S4)–(S7).

2.3. Adsorbent characterization

The morphologies and element compositions of the adsorbents were characterized on a scanning electron microscope (SEM, Gemini SEM 500, Zeiss, Germany) and a transmission electron microscopy (TEM, JEM-2100Plus, Japan) with an energy dispersive X-ray spectrometer (EDX). The X-ray diffraction (XRD) patterns of the adsorbents were collected on a diffractometer (XRD, PANalytical, the Netherlands) with Cu Ka radiation of 1.5418 Å in the 2θ range of 10°-90°. The average size of the crystallite was calculated according to the Scherrer's equation: Ds = Kλ/βcosθ, where Ds is the mean size of the ordered (crystalline) domains; K is a constant that depends on the morphology of crystallites, usually assumed as unity; λ is the X-ray wavelength; β is the half width of diffraction peak; θ is the Bragg's angle. The magnetic properties of the adsorbents were measured by using a vibrating sample

magnetometer (VSM, MPMS-SQUID VSM-094 Quantum, USA). The specific surface area, pore volume and pore size of the adsorbents were calculated using the Brunauer-Emmett-Teller (BET) and Barrett-Joyner-Halenda (BJH) method on a Builder SSA-4200 (Beijing, China) at 77 K. The zeta potentials of the adsorbents were determined by a zeta potential analyzer (Zetasizer Nano ZS90, Malvern, UK). Fourier transform infrared spectroscopy (FTIR, Bruker, Germany) was used to analyze the functional groups of the adsorbents in a KBr pellet in the range of 400 and 4000 cm^{-1}. The surface elemental compositions and functional groups were further quantified by X-ray photoelectron spectroscopy (XPS, ESCALAB Xi+, Thermo Fisher Scientific, USA) employing Al Kα radiation. The C 1 s signal at 284.8 eV was used as the reference for analysis.

3. Results and discussion

3.1. Adsorption isotherms

The equilibrium adsorption isotherm is crucial to assess the adsorption performance and affinity towards Sb(V). Fig. 1 illustrates Sb (V) adsorption isotherms on Ce/Fe$_{CP}$-BC, Ce/Fe$_{ST}$-BC, Fe-BC and BC. The adsorption capacity (Q_e) improved with the increase of Sb (V) concentrations for the larger driving force arisen from higher concentration gradient [33]. It was clear that Ce/Fe$_{CP}$-BC exhibited the highest Q_e in conditions of all the Sb(V) concentrations, followed by Ce/Fe$_{ST}$-BC, Fe-BC and BC. The Q_e gradually reached a plateau and achieved a maximum capacity of 25.0 mg/g for Ce/Fe$_{CP}$-BC, which was almost two times and one order of magnitude higher than that of Ce/Fe$_{ST}$-BC and Fe-BC, respectively. This indicated that chemical co-precipitation method was more effective than solvothermal method and the doped Ce played a crucial role during the Sb(V) adsorption in contrast to Fe. The Sb(V) adsorption capacity on Ce/Fe$_{CP}$-BC was higher compared to other adsorbents as reported in literature, such as 10.0 mg/g for $MnFe_2O_4$ [16], 7.5 mg/g for α-FeOOH [34], 11.0 mg/g for α-Fe$_2$O$_3$ [35], and 4.26–24.48 mg/g for biochar derived from Soybean stover [36], which indicated that Ce/Fe$_{CP}$-BC could be selected as a promising candidate for Sb(V) removal from aqueous solution.

Three equilibrium adsorption isotherm equations, Langmuir, Freundlich and Dubinin–Radushkevich isotherm (D-R), were applied to evaluate the nature of the adsorption process and the relevant parameters were provided in Table S1. The Langmuir model supposes that the adsorption process occurs at homogeneous surfaces with ion exchange as the dominating mechanism, while the Freundlich model suggests multilayer heterogeneous adsorptions and adsorption-complexation interactions dominate the sorption process. According to the correlation coefficient, the isotherm data of Ce/Fe$_{CP}$-BC and Ce/

Fe$_{ST}$-BC could be better fitted by Freundlich model, while that of Fe-BC was better matched by Langmuir model. This indicated that the adsorption of Sb(V) on Ce/Fe$_{CP}$-BC and Ce/Fe$_{ST}$-BC occurred via a chemical and multiple layer process, while on Fe-BC was a physical and monolayer process. Compared to Fe-BC and BC, the value of 1/n (1/n < 0.5) indicated that Sb(V) ions were favorably adsorbed onto the surface of Ce/Fe$_{CP}$-BC and Ce/Fe$_{ST}$-BC [37]. The D-R model could identify whether the adsorption is rate-limited by physical or chemical absorption based on the value of mean adsorption energy E (kJ/mol) [10]. The E values of Ce/Fe$_{CP}$-BC and Ce/Fe$_{ST}$-BC were 11.54 and 8.49 kJ/mol, respectively, while that of Fe-BC was lower than 8.0 kJ/mol. This further confirmed that the adsorption of Sb(V) on Ce/Fe$_{CP}$-BC and Ce/Fe$_{ST}$-BC was chemical adsorption in nature while on Fe-BC was physical adsorption [10].

3.2. Adsorption kinetics

The study of adsorption kinetics is essential to evaluate the adsorption efficiency as well as to expound the mechanism of the adsorption reaction. As can be seen in Fig. 2A, the adsorption of Sb(V) on Ce/Fe$_{CP}$-BC and Ce/Fe$_{ST}$-BC was rapid in the first 160 min, with about 80% of equilibrium adsorption capacity achieved because of the substantial binding sites and high concentration gradient. Then the adsorption rate gradually slowed down and equilibrium was reached at 600 min. Therefore, 900 min was applicable for other equilibrium experiments. The Sb(V) adsorption capacity of Ce/Fe$_{CP}$-BC displayed approximately twice as much as that of Ce/Fe$_{ST}$-BC.

Four classic adsorption kinetic models, the pseudo-first order, pseudo-second order, Elovich and intraparticle diffusion models were applied to fit the experimental data, with their parameters recorded in Table S2. For both Ce/Fe$_{CP}$-BC and Ce/Fe$_{ST}$-BC, the adsorption kinetic data can be best fitted by the pseudo-second order model due to the highest correlation coefficients (R^2) and the closest values between the calculated adsorption capacities ($Q_{e,cal}$) and the experimental values ($Q_{e,exp}$). This indicated that chemisorption was the rate-limiting step of Sb(V) adsorption on Ce/Fe$_{CP}$-BC and Ce/Fe$_{ST}$-BC. The intraparticle diffusion model (Fig. 2B) revealed that the adsorption process occurred in two steps: boundary layer diffusion on the surface of the adsorbents and intra-particle diffusion when the binding sites on the outer surface reached saturation [28]. As linear portion did not pass through the origin, the adsorption of Sb(V) on Ce/Fe$_{CP}$-BC and Ce/Fe$_{ST}$-BC encompassed other steps.

3.3. Effect of pH and coexisting anions on Sb(V) adsorption

The effects of pH on the adsorption of Sb(V) on Ce/Fe$_{CP}$-BC and Ce/Fe$_{ST}$-BC were investigated and the results were depicted in Fig. 3A. It was evident that the adsorption capacity decreased with the increase of solution pH, with Ce/Fe$_{CP}$-BC maintaining higher adsorption capacity than Ce/Fe$_{ST}$-BC over a wide range of pH (2−12). The results regarding the optimum pH for Sb(V) removal were in agreement with literature reports [16,25,38]. The solution pH has a profound effect on the adsorption performance for it would influence the surface charge of adsorbents as well as metallic species [9]. Ce/Fe$_{CP}$-BC and Ce/Fe$_{ST}$-BC possessed pH$_{PZC}$ values of 5.8 and 4.5, respectively (Table 1), and the $[Sb(OH)_6]^-$ is the only dominating species at pH > 2.0. At low pH < pH$_{PZC}$, the hydroxyl groups on the adsorbent surface was protonated and formed an electron positive potential, which facilitated the adsorption of anionic $[Sb(OH)_6]^-$ via electrostatic attraction. When the solution pH is higher than pH$_{PZC}$, the adsorption of Sb(V) was suppressed due to the electrostatic repulsion between the negative charged surface sites and $[Sb(OH)_6]^-$ as well as the competition from hydroxyls (OH^-).

Several anions (Cl^-, SO_4^{2-}, NO_3^-, HCO_3^-, $H_2PO_4^-$) often coexist in natural water and can compete with Sb(V) for the surface active sites of the adsorbents. Therefore, it is necessary to investigate the effect of coexisting anions on Sb(V) adsorption of Ce/Fe$_{CP}$-BC and Ce/Fe$_{ST}$-BC
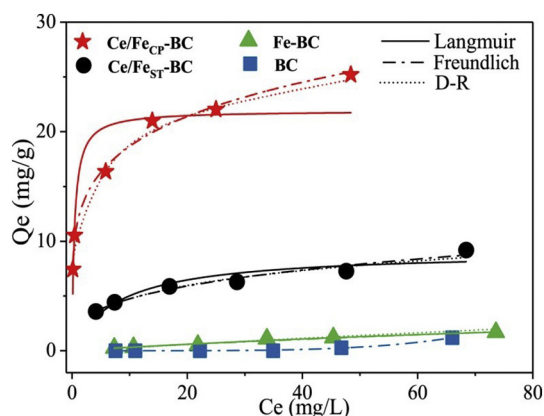
Fig. 1. Adsorption isotherms for Sb(V) adsorption on the adsorbents. The dots and lines represent the experimental data and fitting curves of calculated models, respectively. Experimental conditions: initial C_0 10–100 mg/L, contact time 15 h, dosage 1.0 g/L, initial pH 7.5, temperature 25 ± 1 °C.
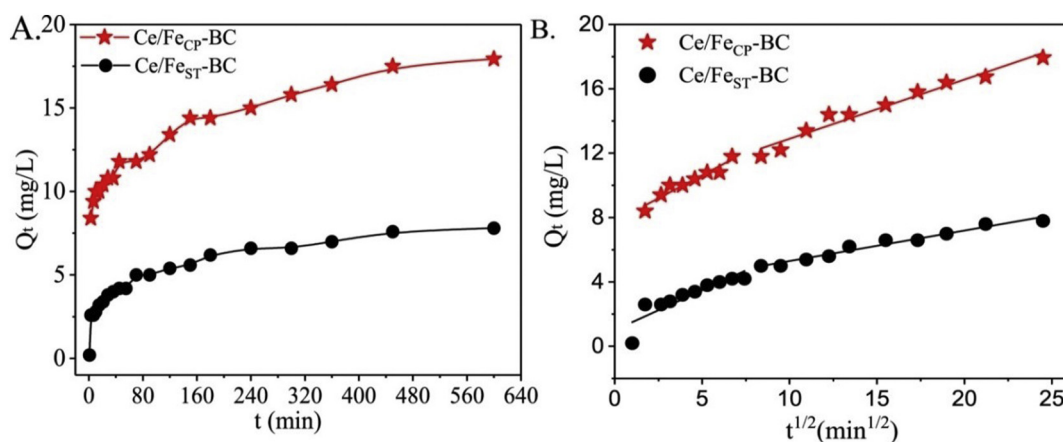
Fig. 2. Effect of contact time (A) and intraparticle diffusion kinetic model (B) for Sb(V) adsorption on Ce/Fe$_{CP}$-BC and Ce/Fe$_{ST}$-BC. Experimental conditions: initial C$_0$ 50 mg/L, dosage 1.0 g/L, initial pH 7.5, temperature 25 ± 1 °C.

(Fig. 3B). For both Ce/Fe$_{CP}$-BC and Ce/Fe$_{ST}$-BC, the presence of Cl$^-$, SO$_4^{2-}$ or NO$_3^-$ had negligible influence on the adsorption capacity due to the less binding energy than Sb(V) [28]. However, HCO$_3^-$ and H$_2$PO$_4^-$ exhibited inhibitory effects on Sb(V) removal, for which a significant reduction of 50% and 74% were found with the presence of phosphate for Ce/Fe$_{CP}$-BC and Ce/Fe$_{ST}$-BC, respectively. The decrease can be attributed to the competition for adsorption active sites between HCO$_3^-$/H$_2$PO$_4^-$ and Sb(V). The influence of H$_2$PO$_4^-$ on the decline of Sb(V) removal was more obvious than HCO$_3^-$, which was likely due to the higher affinity of H$_2$PO$_4^-$ towards Ce active sites [39,40].

3.4. Characterization of the modified Biochars

The morphologies and structures of Fe-BC, Ce/Fe$_{CP}$-BC and Ce/Fe$_{ST}$-BC were characterized by SEM and TEM. The surface of Fe-BC was relatively smooth with distinct macroporous structure (Fig. 4). After modification of different methods, small differences were observed in the surface morphology of Ce/Fe$_{CP}$-BC and Ce/Fe$_{ST}$-BC. A group of large particles were deposited on the surface of Ce/Fe$_{CP}$-BC, which made the surface rough and irregular. In comparison, some small crystals, which were clearly visible at high magnification, were formed on the surface of Ce/Fe$_{ST}$-BC. The TEM-EDX mapping images showed that Fe and Ce elements were homogeneously dispersed in the whole Ce/Fe$_{CP}$-BC and Ce/Fe$_{ST}$-BC, with the weight percentage of 12.13%, 5.68% and 9.22%, 4.55%, respectively (Table 1). All these confirmed that Fe and Ce nanoparticles were successfully loaded on BC's surface.

The porous structure analysis of all the adsorbents was determined and the parameters were presented in Table 1. The S$_{BET}$ and V$_{tot}$ of the Fe-BC were higher compared to those of BC, owing to the introduction of Fe ions. The Ce/Fe$_{CP}$-BC and Ce/Fe$_{ST}$-BC had similar BET surface area to Fe-BC, but lower average pore diameters. The introduction of Ce ions could render the surfaces to be rough and folded, thus decreasing the average pore diameter consequentially. The zeta potentials of the adsorbent suspensions were measured (Fig. S2) and their point of zero charges (pH$_{PZC}$) were provided in Table 1. The BC had a low pH$_{PZC}$ of 2.3, which was not favorable for Sb(V) adsorption, hence the adsorption of Sb(V) on BC in neutral solution was almost negligible. The pH$_{PZC}$ of Fe-BC was found to be 4.3 and the value increased to 4.5–5.8 after the introduction of Ce ions. The Ce/Fe$_{CP}$-BC had higher pH$_{PZC}$ than that of Ce/Fe$_{ST}$-BC, thereby resulting in higher adsorption capacity due to the stronger electrostatic attraction for negative adsorbate Sb(V) in acid and neutral solutions.

The crystal structures of Fe-BC, Ce/Fe$_{CP}$-BC and Ce/Fe$_{ST}$-BC before and after Sb(V) adsorption were characterized and their XRD patterns were illustrated in Fig. 5A. The Fe-BC had five major peaks at 30.10°, 35.45°, 43.08 °, 56.98° and 62.57°, which attributed to (220), (311), (400), (511), and (440) crystal planes of magnetite, respectively [41]. The strong and sharp reflections of XRD peaks in Fe-BC suggested the formation of magnetite crystallites in amorphous biochar matrix. However, after modified with Ce ions, the magnetite displayed weaker diffraction intensity peaks in Ce/Fe$_{CP}$-BC and Ce/Fe$_{ST}$-BC, with their positions changed, indicating that the Ce ion addition significantly influenced the crystallization of magnetite. No obvious peaks of cerium
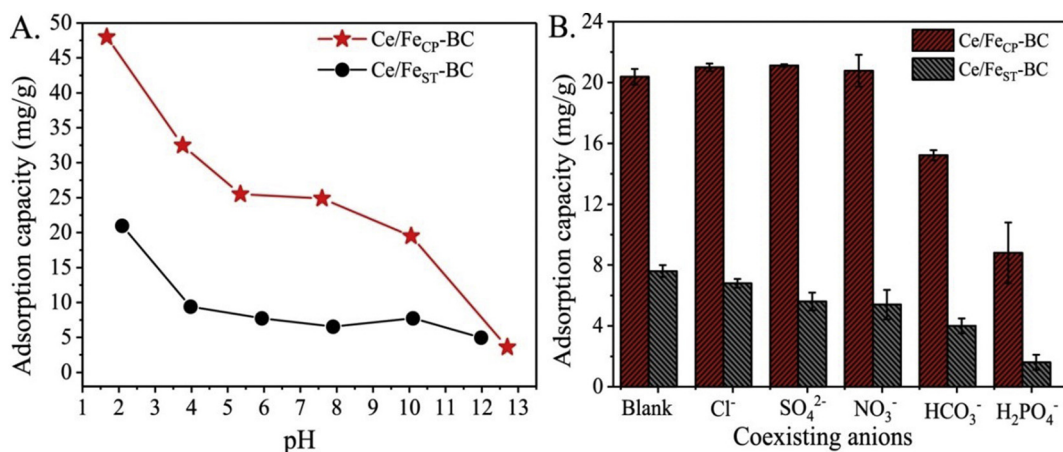
Fig. 3. Effect of solution pH (A) and coexisting anions (B) for Sb(V) adsorption on Ce/Fe$_{CP}$-BC and Ce/Fe$_{ST}$-BC. Experimental conditions in A: dosage 1.0 g/L, temperature 25 ± 1 °C, initial Sb(V) C$_0$ 50 mg/L, and contact time 15 h; Experimental conditions in B: dosage 1.0 g/L, temperature 25 ± 1 °C, initial Sb(V) and anions C$_0$ 50 mg/L, initial pH 7.5 and contact time 15 h.

Table 1
General characteristic of the adsorbents.

	BC	Fe-BC	Ce/Fe$_{CP}$- BC	Ce/Fe$_{ST}$–BC
C (wt%)	68.00	77.90	53.92	61.90
Fe (wt%)	–	7.02	12.13	9.22
Ce (wt%)	–	–	5.68	4.55
[a]S$_{BET}$ (m²/g)	111.2	232.69	230.65	269.9
[b]V$_{tot}$ (cm³/g)	0.19	0.28	0.19	0.22
[c]D$_p$ (nm)	6.98	4.78	3.33	3.28
[d]pH$_{PZC}$	2.3	4.3	5.8	4.5
(311) Peak Position (°)	–	35.448	35.581	35.645
(311) peak shift (°)	–	0.006	−0.127	−0.191
Crystalline size (nm)	–	13.0	17.3	23.3
Saturated magnetization (emu/g)	0.00	5.00	0.93	2.11

[a] S$_{BET}$: BET surface area was determined by using the Brunauer–Emmett–Teller (BET) theory;
[b] V$_{tot}$: total pore volume was determined using density functional theory (DFT) method;
[c] D$_p$: average pore diameter was calculated as D$_p$ = 4V$_{tot}$/S$_{BET}$;
[d] pH$_{PZC}$: Point of zero charge of adsorbent.

oxide were observed in the samples of Ce/Fe$_{CP}$-BC and Ce/Fe$_{ST}$-BC, indicative of the probable amorphous forms of cerium oxide. The crystalline sizes of Ce/Fe$_{CP}$-BC and Ce/Fe$_{ST}$-BC were higher than that of Fe-BC (Table 1), suggesting that Ce ions were doped into the lattice of magnetite as Ce^{3+} ions (115.0 pm) had larger ionic radius than Fe^{3+} ions (78.5 pm). The combined form of the spinel structure in a lattice cell was assumed based on relevant researches (Fig. 6.) [25,42]. After the adsorption of Sb(V) ions, the peak intensity of Fe-BC, Ce/Fe$_{CP}$-BC and Ce/Fe$_{ST}$-BC further weakened slightly, implying chemical interactions between Ce/Fe and Sb(V) to realize enhanced adsorption.

The magnetic performance of modified BCs was characterized by magnetic hysteresis loop (Fig. 1S) and their saturated magnetizations were listed in Table 1. The magnetic saturations (Ms) of Ce/Fe$_{CP}$-BC and Ce/Fe$_{ST}$-BC were 0.93 and 2.11 emu/g, respectively, which were lower than that of Fe-BC. The reduction in Ms. after doping with Ce

ions was contributed to the disrupted crystallinity of magnetite, which was consistent with XRD analysis. The solvothermal method could provide a more reductive condition, which was more suitable for the formation of crystallinity than co-precipitation method. Therefore, Ce/Fe$_{ST}$-BC had higher Ms. than Ce/Fe$_{CP}$-BC. Although the Ms. decreased after doping with ions, it was in the range as reported in literature (0.05–68.2 emu/g).

The FTIR spectra of the samples before and after Sb(V) adsorption were obtained to determine the presence of various functional groups on the adsorbents. The Fe-BC, Ce/Fe$_{CP}$-BC and Ce/Fe$_{ST}$-BC had similar infrared absorption bands as displayed in Fig. 5B. All the adsorbents contained large amounts of –OH as located between 3500 and 3304 cm^{-1} [43,44]. In the spectrum of Fe-BC, a strong characteristic peak at 580 cm^{-1} for the Fe—O vibration of magnetite was observed, further confirming the formation of magnetite on BC's surface [25]. In the spectrum of Ce/Fe$_{CP}$-BC and Ce/Fe$_{ST}$-BC, no obvious Ce band was identified probably due to low Ce loading content. Besides, the Fe—O band almost disappeared after doping Ce ions via either co-precipitation or solvothermal method, indicating that the crystal structure of magnetite was destroyed [45]. After Sb(V) adsorption, the spectrum of Fe-BC did not change much except that the intensity of Fe—O band markedly weakened, revealing formation of Fe–O–Sb complexes on Fe-BC surfaces as has been previously observed in literature [46]. For Ce/Fe$_{CP}$-BC and Ce/Fe$_{ST}$-BC, the intensity of –OH band at 3048 cm^{-1} significantly increased and the peak position showed an obvious red-shift after Sb(V) adsorption, which could be caused by the –OH in the adsorbed Sb(V) species.

The surface functional groups on the adsorbents as well as the mechanisms were further elucidated by XPS analysis. The full survey XPS spectrum illustrated that the main compositions of Fe-BC, Ce/Fe$_{CP}$-BC and Ce/Fe$_{ST}$-BC were C and O (Fig. 5C), which were consistent with EDS analysis (Table 1). Fe element was detected in all three adsorbents and a new peak corresponding to Ce element was observed on Ce/Fe$_{CP}$-BC and Ce/Fe$_{ST}$-BC, which further validated that Ce ions were successfully loaded on BC' s surface. The newly emerged Sb 3d spectra at
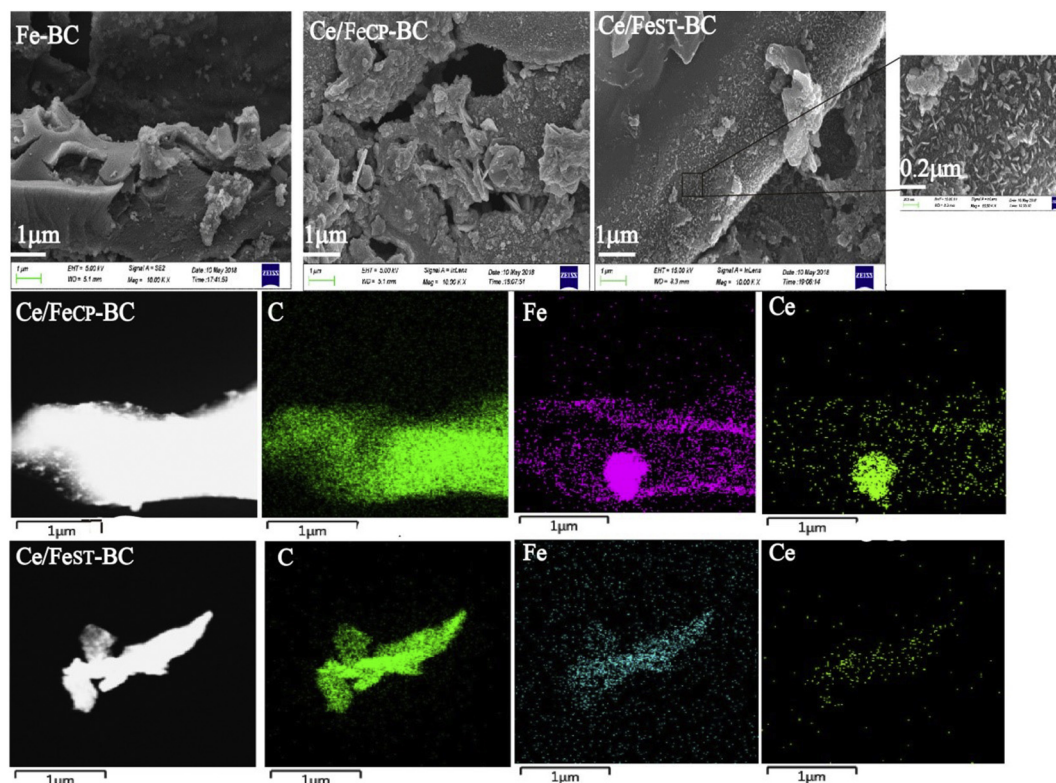
Fig. 4. The first line is the SEM images of Fe-BC, Ce/Fe$_{CP}$-BC and Ce/Fe$_{ST}$-BC, the second and third lines are TEM of Ce/Fe$_{CP}$-BC and Ce/Fe$_{ST}$-BC and their C, Fe, Ce elemental mapping images.
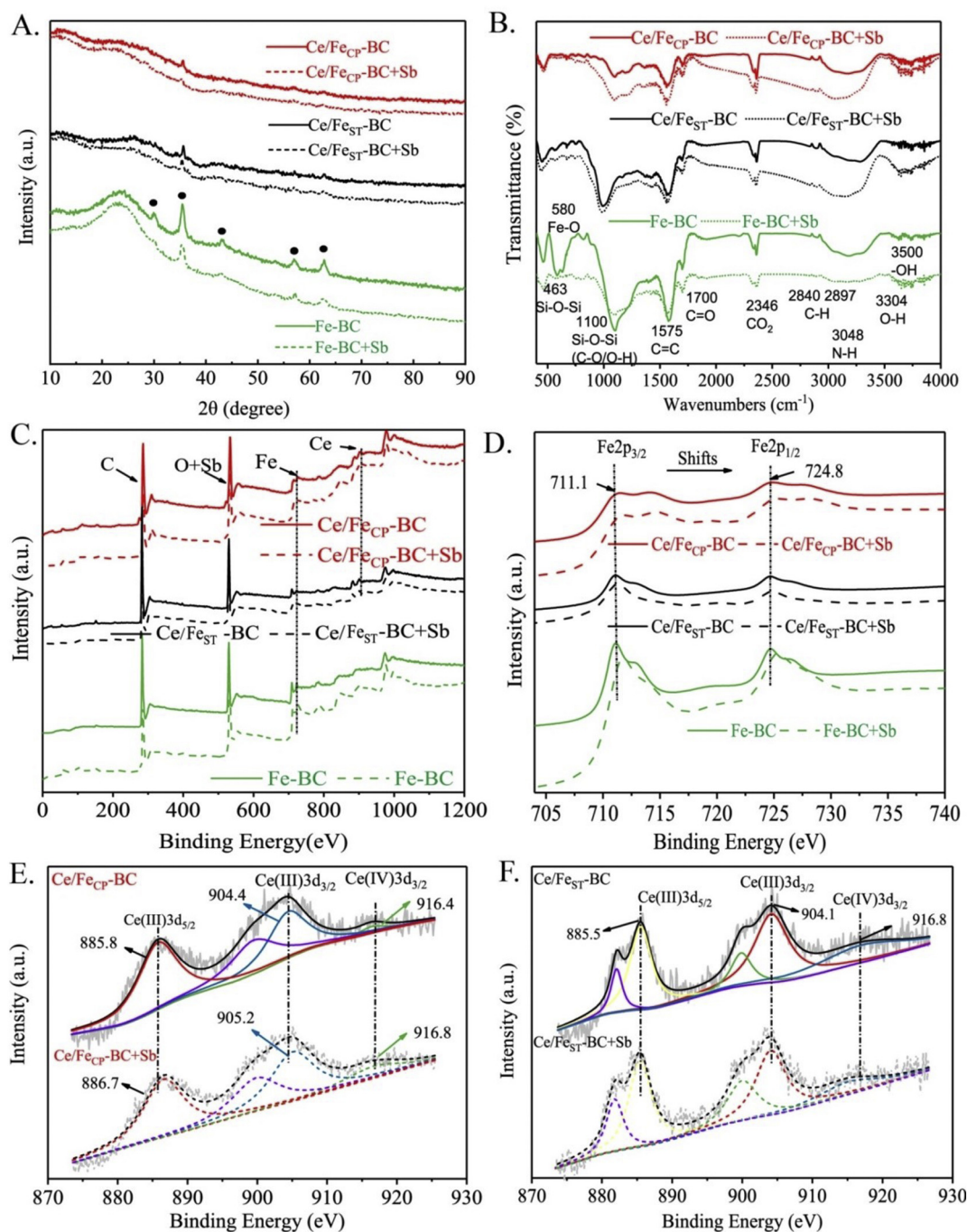
Fig. 5. XRD patterns (A), FTIR spectra (B) and XPS spectra (C) of the adsorbents before and after Sb(V) adsorption for Fe-BC, Ce/Fe$_{CP}$-BC and Ce/Fe$_{ST}$-BC. The Fe 2p$_{3/2}$ and Fe 2p$_{1/2}$ spectra (D) and Ce 3d$_{5/2}$, Ce 3d$_{3/2}$ spectra of Ce/Fe$_{CP}$-BC (E) and Ce/Fe$_{ST}$-BC (F) before and after Sb(V) adsorption.

540.5 eV after Sb(V) adsorption implied the successful Sb loading on the adsorbents.

The high resolution scan of O 1 s spectra of Fe-BC, Ce/Fe$_{CP}$-BC and Ce/Fe$_{ST}$-BC could be deconvoluted into three peaks of lattice oxygen, M–O (528.9–530.6 eV), hydroxyl groups, M–OH (531.6–533.0 eV) and adsorbed water (533.0–535.6 eV) [28,47] as shown in Fig. S3. The relative content of each component was calculated based on the peak area and was presented in Table 2. The Fe-BC and Ce/Fe$_{CP}$-BC had similar oxygen distributions and possessed considerable amounts of M–OH with high ratios of 72.32% and 72.33%, respectively. The Ce/Fe$_{ST}$-BC had lower content of M–OH but higher content of M-O compared to the other two adsorbents, indicating more cerium oxides were formed in the course of solvothermal synthesis than co-precipitation process.

After the Sb(V) adsorption, the percentage of M–OH in Ce/Fe$_{CP}$-BC dramatically decreased to 60.56%, while the ratio of M–O almost increased in the same proportion as M–OH. This was likely caused by the replacement of hydroxyl groups on Sb(V) species via ligand exchange, with the formation of M–O–Sb after adsorption [47]. Although an obvious reduction was also observed for M–OH in Fe-BC, the ratio of M–O did not change after adsorption. This indicated that no Fe–O–Sb complex was formed and M–OH decrease was caused by the formation of hydrogen bonding with Sb(V) species. For Ce/Fe$_{ST}$-BC, the oxygen species showed no obvious changes after adsorption, indicating that other mechanisms were involved.

The high resolution XPS spectra of Fe 2p before and after adsorption were displayed in Fig. 5D. The Fe-BC contained two
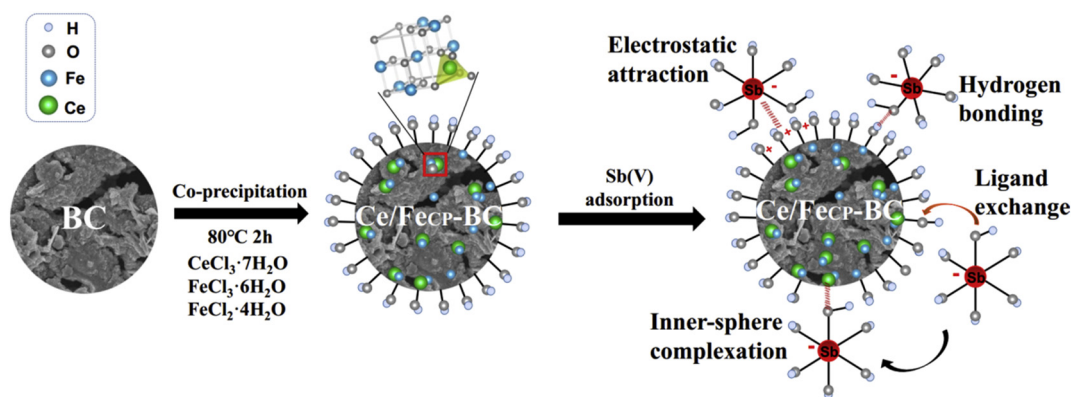
Fig. 6. Schematic diagram of the formation of Ce/Fe$_{CP}$-BC and its mechanisms for Sb(V) adsorption.

major peaks at approximately 711.1 and 724.8 eV [48,49], which were assigned to Fe 2p$_{3/2}$ and Fe 2p$_{1/2}$ of standard magnetite, respectively. The Ce/Fe$_{ST}$–BC exhibited similar Fe 2p peaks but with lower intensity compared to Fe-BC, suggesting lower magnetite content after doped with Ce ions via solvothermal method. For Ce/Fe$_{CP}$-BC, the intensity of Fe 2p$_{3/2}$ decreased and its position shifted slightly to higher binding energy sides, indicating that Ce ions were doped into magnetite structure via co-precipitation method [50]. After Sb(V) adsorption, the Fe 2p spectra of all the adsorbents did not change much, which further confirmed that Fe–O–Sb complex was not formed during the adsorption process.

The XPS spectrum of Ce 3d in both Ce/Fe$_{CP}$-BC and Ce/Fe$_{ST}$–BC exhibited two major peaks of Ce 3d$_{5/2}$and Ce 3d$_{3/2}$ that located at 885.8 and 904.1 eV, respectively (Fig. 5 E and F) [25], indicating that the dominating chemical state of Ce was Ce^{3+}. A weak peak located at 916.8 eV (Ce^{5+}) also existed, possibly due to the oxidization by the oxygen containing groups on BC's surface during the synthesis process. After Sb(V) adsorption, the peaks of Ce 3d in Ce/Fe$_{CP}$-BC shifted to higher binding energy, implying the formation of new Ce–O–Sb inner-sphere complex. However, no apparent changes were found in Ce/Fe$_{ST}$–BC. This was probably because the Ce element was crystallized during the solvothermal process, which was not beneficial for the formation of Ce–O–Sb complex and resulted in a low Sb(V) adsorption capacity. Therefore, the formation of Ce–O–Sb complex was the main contribution to the Sb(V) adsorption enhancement in Ce/Fe$_{CP}$-BC.

3.5. Adsorption mechanisms of Ce/Fe$_{CP}$-BC

Based on the synthesis procedure of Ce/Fe$_{CP}$-BC and the results from the adsorption performance and physiochemical analyses, the mechanisms involved in the Sb(V) adsorption on Ce/Fe$_{CP}$-BC were illustrated in Fig. 6. The adsorption capacity in Ce/Fe$_{CP}$-BC was one order of magnitude higher than that of Fe-BC, indicating the crucial role of Ce element in Sb(V) adsorption enhancement. The combined results of XRD, FTIR and XPS analyses revealed that Ce ions were far more likely to be doped into the structure of magnetite and large amounts of –OH were

generated on the surface of Ce/Fe$_{CP}$-BC after the co-precipitation method. In the enlarged view of Ce/Fe$_{CP}$-BC, one Ce^{3+} ion replaced Fe^{3+} at octahedral sites in a lattice structure, which was speculated according to relevant researches in Ce^{III}-doped Fe$_3$O$_4$ magnetic particles [25] and cobalt ferrites [51]. After the Sb(V) adsorption, the abundant presence of –OH on Ce/Fe$_{CP}$-BC was replaced by the Sb(V) species via ligand exchange [47] in accordance with the decreased content of M–OH species, and the subsequently formed inner-sphere surface complex can be demonstrated by the increased content of M–O species as well as the positive shifts of Ce 3d XPS spectra. Meanwhile, the –OH on the surface of Ce/Fe$_{CP}$-BC could act as H-donor and formed hydrogen bonding with the oxygen atom of the Sb(V) complex (H-acceptor) [52]. At low solution pH, the deprotonation of hydroxyl groups could adsorb the negative adsorbate [Sb(OH)$_6$]$^-$ via electrostatic attraction. Among these mechanisms, the ligand exchange and the formation of Ce–O–Sb complex were the main contributions to the significant Sb(V) adsorption increment on Ce/Fe$_{CP}$-BC.

4. Conclusions

In this work, two methods (chemical co-precipitation and solvothermal method) were used to synthesize Ce-doped magnetic biochars. The chemical co-precipitation method was more effective than solvothermal method in this system for Sb(V) removal, with Ce/Fe$_{CP}$-BC exhibiting a higher adsorption capacity of 25.0 mg/g than Ce/Fe$_{ST}$-BC and Fe-BC. The Sb(V) adsorption capacity on Ce/Fe$_{CP}$-BC was high at acid conditions due to the electrostatic attraction. The presence of coexisting anions had negligible effect on Sb(V) adsorption except HCO$_3^-$ and H$_2$PO$_4^-$. The combined results of physiochemical characterizations demonstrated that Ce atoms were successfully doped into magnetite structure and abundant hydroxyl groups were formed on the surface of Ce/Fe$_{CP}$-BC, which played a dominant role in the adsorption enhancement. Based on the analyses, the adsorption mechanisms included the formation of Ce–O–Sb inner-sphere surface complex, hydrogen bonding, electrostatic attraction and ligand exchange, and the inner-sphere complexation was the dominant contribution. The high Sb(V) adsorption performance indicated that Ce/Fe$_{CP}$-BC could be used as a promising adsorbent candidate for Sb(V) removal in aqueous solution.

Table 2
Distribution (%) of oxygen forms of the adsorbents before and after Sb(V) adsorption.

Samples	M-O	M-OH	H$_2$O (ads)
	528.9–530.6 eV	531.6–533.0 eV	533.0–535.6 eV
Fe-BC	11.66	72.32	16.02
Ce/Fe$_{CP}$-BC	11.65	72.33	16.02
Ce/Fe$_{ST}$–BC	21.22	49.58	29.20
Fe-BC + Sb	11.70	64.77	23.52
Ce/Fe$_{CP}$-BC + Sb	25.06	60.56	14.38
Ce/Fe$_{ST}$–BC + Sb	21.54	50.90	27.56

Appendix A. Supplementary data

Supplementary data to this article can be found online at https://doi.org/10.1016/j.powtec.2019.01.022.

References

[1] L. Han, H. Sun, K.S. Ro, K. Sun, J.A. Libra, B. Xing, Removal of antimony (III) and cadmium (II) from aqueous solution using animal manure-derived hydrochars and pyrochars, Bioresour. Technol. 234 (2017) 77–85.
[2] M. Filella, N. Belzile, Y.W. Chen, Antimony in the environment: a review focused on natural waters I. Occurrence, Earth-Sci. Rev. 57 (2002) 125–176.
[3] J. Luo, X. Luo, J. Crittenden, J. Qu, Y. Bai, Y. Peng, J. Li, Removal of antimonite (Sb(III)) and antimonate (Sb(V)) from aqueous solution using carbon nanofibers that are decorated with zirconium oxide (ZrO2), Environ. Sci. Technol. 49 (2015) 11115–11124.
[4] Y.-Y. Wang, H.-Y. Ji, H.-H. Lu, Y.-X. Liu, R.-Q. Yang, L.-L. He, S.-M. Yang, Simultaneous removal of Sb(III) and Cd(II) in water by adsorption onto a MnFe2O4 biochar nano-composite, RSC Adv. 8 (2018) 3264–3273.
[5] J. Li, B. Zheng, Y. He, Y. Zhou, X. Chen, S. Ruan, Y. Yang, C. Dai, L. Tang, Antimony contamination, consequences and removal techniques: a review, Ecotoxicol. Environ. Saf. 156 (2018) 125–134.
[6] S.Y. Pu, H. Ma, A. Zinchenko, W. Chu, Novel highly porous magnetic hydrogel beads composed of chitosan and sodium citrate: an effective adsorbent for the removal of heavy metals from aqueous solutions, Environ. Sci. Pollut. Res. 24 (2017) 16520–16530.
[7] L. Wang, H. Wen, L. Li, Scale dependence of surface complexation capacity and rates in heterogeneous media, Sci. Total Environ. 635 (2018) 1547–1555.
[8] Q. Shi, A. Terracciano, Y. Zhao, C. Wei, C. Christodoulatos, X. Meng, Evaluation of metal oxides and activated carbon for lead removal: Kinetics, isotherms, column tests, and the role of co-existing ions, Sci. Total Environ. 648 (2019) 176–183.
[9] J. Ifthikar, X. Jiao, A. Ngambia, T. Wang, A. Khan, A. Jawad, Q. Xue, L. Liu, Z.Q. Chen, Facile One-pot synthesis of sustainable carboxymethyl chitosan - sewage sludge biochar for effective heavy metal chelation and regeneration, Bioresour. Technol. 262 (2018) 22–31.
[10] M.K. Luo, H. Lin, B. Li, Y.B. Dong, Y.H. He, L. Wang, A novel modification of lignin on corncob-based biochar to enhance removal of cadmium from water, Bioresour. Technol. 259 (2018) 312–318.
[11] Q. Yin, H. Ren, R. Wang, Z. Zhao, Evaluation of nitrate and phosphate adsorption on Al-modified biochar: Influence of Al content, Sci. Total Environ. 631-632 (2018) 895–903.
[12] M.B. Ahmed, J.L. Zhou, H.H. Ngo, W. Guo, M. Chen, Progress in the preparation and application of modified biochar for improved contaminant removal from water and wastewater, Bioresour. Technol. 214 (2016) 836–851.
[13] Z. Ren, X. Xu, X. Wang, B. Gao, Q. Yue, W. Song, L. Zhang, H. Wang, FTIR, Raman, and XPS analysis during phosphate, nitrate and Cr(VI) removal by amine cross-linking biosorbent, J. Colloid Interface Sci. 468 (2016) 313–323.
[14] M. Vithanage, A.U. Rajapaksha, M. Ahmad, M. Uchimiya, X. Dou, D.S. Alessi, Y.S. Ok, Mechanisms of antimony adsorption onto soybean stover-derived biochar in aqueous solutions, J. Environ. Manag. 151 (2015) 443–449.
[15] X. Hu, Z. Ding, A.R. Zimmerman, S. Wang, B. Gao, Batch and column sorption of arsenic onto iron-impregnated biochar synthesized through hydrolysis, Water Res. 68 (2015) 206–216.
[16] Z. Qi, T.P. Joshi, R. Liu, Y. Li, H. Liu, J. Qu, Adsorption combined with superconducting high gradient magnetic separation technique used for removal of arsenic and antimony, J. Hazard. Mater. 343 (2018) 36–48.
[17] S.Q. Shi, J.K. Yang, S. Liang, M.Y. Li, Q. Gan, K.K. Xiao, J.P. Hu, Enhanced Cr(VI) removal from acidic solutions using biochar modified by Fe3O4@SiO2-NH2 particles, Sci. Total Environ. 628-629 (2018) 499–508.
[18] E.B. Son, K.M. Poo, J.S. Chang, K.J. Chae, Heavy metal removal from aqueous solutions using engineered magnetic biochars derived from waste marine macro-algal biomass, Sci. Total Environ. 615 (2018) 161–168.
[19] Q. Wang, X. Wang, W. Luo, J. Sun, Q. Xu, F. Chen, J. Zhao, S. Wang, F. Yao, D. Wang, X. Li, G. Zeng, Effectiveness and mechanisms of phosphate adsorption on iron-modified biochars derived from waste activated sludge, Bioresour. Technol. 247 (2018) 537–544.
[20] L.-K. Wu, Y.-Y. Li, H.-Z. Cao, G.-Q. Zheng, Copper-promoted cementation of antimony in hydrochloric acid system: a green protocol, J. Hazard. Mater. 299 (2015) 520–528.
[21] R. Liu, W. Xu, Z. He, H. Lan, H. Liu, J. Qu, T. Prasai, Adsorption of antimony(V) onto Mn(II)-enriched surfaces of manganese-oxide and Fe-Mn binary oxide, Chemosphere 138 (2015) 616–624.
[22] L. Wang, J. Wang, Z. Wang, C. He, W. Lyu, W. Yan, L. Yang, Enhanced antimonate (Sb(V)) removal from aqueous solution by La-doped magnetic biochars, Chem. Eng. J. 354 (2018) 623–632.
[23] X. Li, X. Dou, J. Li, Antimony(V) removal from water by iron-zirconium bimetal oxide: performance and mechanism, J. Environ. Sci. 24 (2012) 1197–1203.
[24] Z. Qi, H. Lan, T.P. Joshi, R. Liu, H. Liu, J. Qu, Enhanced oxidative and adsorptive capability towards antimony by copper-doping into magnetite magnetic particles, RSC Adv. 6 (2016) 66990–67001.
[25] Z. Qi, T.P. Joshi, R. Liu, H. Liu, J. Qu, Synthesis of Ce(III)-doped Fe3O4 magnetic particles for efficient removal of antimony from aqueous solution, J. Hazard. Mater. 329 (2017) 193–204.
[26] H. Qiu, C. Liang, J. Yu, Q. Zhang, M. Song, F. Chen, Preferable phosphate sequestration by nano-La(III) (hydr)oxides modified wheat straw with excellent properties in regeneration, Chem. Eng. J. 315 (2017) 345–354.
[27] P.K. Mishra, R. Kumar, P.K. Rai, Surfactant-freeone-pot synthesis of CeO2, TiO2 and Ti@Ce oxide nanoparticles for the ultrafast removal of Cr(VI) from aqueous media, Nanoscale 10 (2018) 7257–7269.
[28] Z.P. Wen, J. Ke, J.L. Xu, S. Guo, Y.L. Zhang, R. Chen, One-step facile hydrothermal synthesis of flowerlike Ce/Fe bimetallic oxides for efficient as(V) and Cr(VI) remediation: performance and mechanism, Chem. Eng. J. 343 (2018) 416–426.
[29] Y. Zhang, M. Yang, X.M. Dou, H. He, D.S. Wang, Arsenate adsorption on an Fe-Ce bimetal oxide adsorbent: role of surface properties, Environ. Sci. Technol. 39 (2005) 7246–7253.
[30] Q. Zhou, B. Liao, L. Lin, W. Qiu, Z. Song, Adsorption of Cu(II) and Cd(II) from aqueous solutions by ferromanganese binary oxide–biochar composites, Sci. Total Environ. 615 (2018) 115–122.
[31] L. Wang, W. Yan, C. He, H. Wen, Z. Cai, Z.X. Wanga, Z.Z. Chen, W.F. Liu, Microwave-assisted preparation of nitrogen-doped biochars by ammonium acetate activation for adsorption of acid red 18, Appl. Surf. Sci. 433 (2018) 222–231.
[32] L. Wang, Z. Chen, H. Wen, Z. Cai, C. He, Z. Wang, W. Yan, Microwave assisted modification of activated carbons by organic acid ammoniums activation for enhanced adsorption of acid red 18, Powder Technol. 323 (2018) 230–237.
[33] J.J. Zhao, Y.Z. Niu, B. Ren, H. Chen, S.X. Zhang, J. Jin, Y. Zhang, Synthesis of Schiff base functionalized superparamagnetic Fe3O4 composites for effective removal of Pb(II) and Cd(II) from aqueous solution, Chem. Eng. J. 347 (2018) 574–584.
[34] D. Li, X. Hu, Y. Sun, S. Su, A. Xia, H. Ge, Goethite (α-FeOOH) nanopowders synthesized via a surfactant-assisted hydrothermal method: Morphology, magnetic properties and conversion to rice-like α-Fe2O3 after annealing, RSC Adv. 5 (2015).
[35] X. Guo, Z. Wu, M. He, X. Meng, X. Jin, N. Qiu, J. Zhang, Adsorption of antimony onto iron oxyhydroxides: adsorption behavior and surface structure, J. Hazard. Mater. 276 (2014) 339–345.
[36] M. Vithanage, A.U. Rajapaksha, M. Ahmad, M. Uchimiya, X. Dou, D.S. Alessi, S.O. Yong, Mechanisms of antimony adsorption onto soybean stover-derived biochar in aqueous solutions, J. Environ. Manag. 151 (2015) 443–449.
[37] L. Wang, D. Hu, X.K. Kong, J.G. Liu, X.H. Li, K. Zhou, H.G. Zhao, C.H. Zhou, Anionic polypeptide poly(gamma-glutamic acid)-functionalized magnetic Fe3O4-GO-(o-MWCNTs) hybrid nanocomposite for high-efficiency removal of Cd (II), Cu(II) and Ni(II) heavy metal ions, Chem. Eng. J. 346 (2018) 38–49.
[38] L. Wang, J.-m. Wang, R. Zhang, X.-g. Liu, G.-x. Song, X.-f. Chen, Y. Wang, J.-l. Kong, Highly efficient as(V)/Sb(V) removal by magnetic sludge composite: synthesis, characterization, equilibrium, and mechanism studies, RSC Adv. 6 (2016) 42876–42884.
[39] J. Liu, J. Cao, Y. Hu, Y. Han, J. Zhou, Adsorption of phosphate ions from aqueous solutions by a CeO2 functionalized Fe3O4@SiO2 core-shell magnetic nanomaterial, Water Sci. Technol. 76 (2017) 2867–2875.
[40] Y. Feng, Y. Lu, Y. Liu, L. Xue, D.D. Dionysiou, L. Yang, B. Xing, Nano-cerium oxide functionalized biochar for phosphate retention: preparation, optimization and rice paddy application, Chemosphere 185 (2017) 816–825.
[41] J. Ifthikar, J. Wang, Q. Wang, T. Wang, H. Wang, A. Khan, A. Jawad, T. Sun, X. Jiao, Z. Chen, Highly efficient lead distribution by magnetic sewage sludge biochar: sorption mechanisms and bench applications, Bioresour. Technol. 238 (2017) 399–406.
[42] D.H.K. Reddy, Y.-S. Yun, Spinel ferrite magnetic adsorbents: alternative future materials for water purification? Coord. Chem. Rev. 315 (2016) 90–111.
[43] H. Liu, P. Dai, J. Zhang, C.L. Zhang, N. Bao, C. Cheng, L. Ren, Preparation and evaluation of activated carbons from lotus stalk with trimethyl phosphate and tributyl phosphate activation for lead removal, Chem. Eng. J. 228 (2013) 425–434.
[44] A.M. Ebrahim, E. Rodriguez-Castellon, J. Maria Montenegro, T.J. Bandosz, Effect of chemical heterogeneity on photoluminescence of graphite oxide treated with S-/N-containing modifiers, Appl. Surf. Sci. 332 (2015) 272–280.
[45] A.S. Kumar, C. Sharma, Synthesis, characterization and catalytic wet air oxidation property of mesoporous Ce1-xFexO2 mixed oxides, Mater. Chem. Phys. 155 (2015) 223–231.
[46] K.A. McComb, D. Craw, A.J. McQuillan, ATR-IR spectroscopic study of antimonate adsorption to iron oxide, Langmuir 23 (2007) 12125–12130.
[47] Y. Yu, C. Zhang, L. Yang, J.P. Chen, Cerium oxide modified activated carbon as an efficient and effective adsorbent for rapid uptake of arsenate and arsenite: material development and study of performance and mechanisms, Chem. Eng. J. 315 (2017) 630–638.
[48] J. Lu, X. Jiao, D. Chen, W. Li, Solvothermal synthesis and characterization of Fe3O4 and γ-Fe2O3 nanoplates, J. Phys. Chem. C 113 (2009) 4012–4017.
[49] X. Zhang, X. Niu, X. Meng, Y. Li, J. Zhao, Structural evolution and characteristics of the phase transformations between α-Fe2O3, Fe3O4 and γ-Fe2O3 nanoparticles under reducing and oxidizing atmospheres, Cryst. Eng. Comm. 15 (2013) 8166–8172.
[50] L. Fang, R. Liu, J. Li, C. Xu, L.-Z. Huang, D. Wang, Magnetite/Lanthanum hydroxide for phosphate sequestration and recovery from lake and the attenuation effects of sediment particles, Water Res. 130 (2018) 243–254.
[51] S. Zhang, H. Niu, Y. Cai, X. Zhao, Y. Shi, Arsenite and arsenate adsorption on coprecipitated bimetal oxide magnetic nanomaterials: MnFe2O4 and CoFe2O4, Chem. Eng. J. 158 (2010) 599–607.
[52] F. Wang, H. Sun, X. Ren, K. Zhang, Sorption of naphthalene and its hydroxyl substitutes onto biochars in single-solute and bi-solute systems with propranolol as the co-solute, Chem. Eng. J. 326 (2017) 281–291.